

# Microscopic model for $d$ -wave charge-carrier pairing and non-Fermi-liquid behavior in a purely repulsive two-dimensional electron system

Mona Berciu and Sajeev John

*Department of Physics, University of Toronto, 60 St. George Street, Toronto, Ontario, M5S 1A7, Canada*

(Received 27 December 1999; revised manuscript received 28 March 2000)

We investigate a microscopic model for strongly correlated electrons with both on-site and nearest-neighbor Coulomb repulsion on a two-dimensional (2D) square lattice. This exhibits a state in which electrons undergo a “somersault” in their internal spin space (spin flux) as they traverse a closed loop in external coordinate space. When this spin- $\frac{1}{2}$  antiferromagnetic (AFM) insulator is doped, the ground state is a liquid of charged, bosonic meron vortices, which for topological reasons are created in vortex-antivortex pairs. The magnetic exchange energy of the distorted AFM background leads to a logarithmic vortex-antivortex attraction which overcomes the direct Coulomb repulsion between holes localized on the vortex cores. This leads to the appearance of preformed charged pairs. We use the configuration interaction (CI) method to study the quantum translational and rotational motion of various charged magnetic solitons and soliton pairs. The CI method systematically describes fluctuation and quantum tunneling corrections to the Hartree-Fock approximation. We find that the lowest-energy charged meron-antimeron pairs exhibit  $d$ -wave rotational symmetry, consistent with the symmetry of the cuprate superconducting order parameter. For a single hole in the 2D AFM plane, we find a precursor to spin-charge separation in which a conventional charged spin polaron dissociates into a singly charged meron-antimeron bound pair. This model provides a unified microscopic basis for (i) non-Fermi-liquid transport properties, (ii)  $d$ -wave preformed charged carrier pairs, (iii) midinfrared optical absorption, (iv) destruction of AFM long-range order with doping and other magnetic properties, and (v) certain aspects of angle-resolved photoemission spectroscopy.

## I. INTRODUCTION

The microscopic understanding of the effect of charge-carrier doping on spin- $\frac{1}{2}$  antiferromagnetic (AFM) Mott insulators is the central issue of the high-temperature superconducting cuprates.<sup>1</sup> Many puzzling experimental features of these systems<sup>2</sup> suggest that a fundamental law of nature remains to be recognized. Extremely low doping ( $\delta \sim 0.02$ – $0.05$  charge carriers per site) leads to a complete destruction of the long-range AFM order, and a transition to an unusual non-Fermi-liquid metal. This unusual metal becomes superconducting, with the transition temperature  $T_c$  strongly dependent on the doping  $\delta$ . The maximum  $T_c$  is reached for dopings around  $\delta=0.15$ . For higher dopings the critical temperature decreases to zero, and in the overdoped region a crossover toward a (nonsuperconducting) Fermi liquid takes place. Two central questions require resolution. The first one concerns the nature of the charge carriers responsible for this non-Fermi-liquid metallic behavior. This is a fundamental issue, since it lies outside the framework of Landau’s Fermi-liquid theory, and it necessitates understanding the appearance of non-quasiparticle-like charge carriers in a system of interacting electrons. The second question concerns the nature of the strong attractive pairing between these charge carriers, given the purely repulsive interaction between the constituent electrons. In conventional superconductors, the pairing attraction is due to overscreening of the electron-electron Coulomb repulsion by the ionic lattice. In the case of high-temperature superconducting cuprates, it has been suggested<sup>1</sup> that pairing is an intrinsic property of the electron gas itself mediated by AFM spin fluctuations of the

doped system. Accordingly, the challenge is to identify a strong attractive force based purely on repulsive Coulomb interactions. In this paper, we derive such a force, and demonstrate that it leads to  $d$ -wave pairing of charge carrying holes introduced by doping a quantum, spin- $\frac{1}{2}$ , Mott-Hubbard antiferromagnet.

The simplest model Hamiltonians used to investigate the cuprate physics are the Hubbard model and the closely related  $t$ - $J$  model. Unlike the one-dimensional (1D) problem, an exact solution for the 2D Hubbard Hamiltonian is not known. As a result, various approximations are necessary. Although the application of the mean-field theory has been severely criticized in this context, it provides a valuable reference point for incorporating fluctuation effects. Moreover, even for the 1D Hubbard model, essential features of the exact solution may be recaptured by judiciously incorporating fluctuation and tunneling effects into mean-field theory.<sup>3</sup> The most straightforward mean-field theory is the Hartree-Fock approximation (HFA). At half-filling ( $\delta=0$ ) the HFA predicts an AFM Mott insulator ground state. As the system is doped, the HFA suggests that charge-carrier holes in the AFM background assemble in charged stripes, which are quasi-one-dimensional structures.<sup>4–6</sup> A large effort has been devoted to studying these charged stripes and relating them to certain features of the cuprates.<sup>7</sup>

Recently, a more fundamental investigation of the many-electron problem has suggested the possibility of an alternative model Hamiltonian for the cuprate physics. This model Hamiltonian, called the spin-flux model,<sup>8</sup> suggests that the long-range Coulomb interaction between spin- $\frac{1}{2}$  electrons leads to qualitatively new physics, not apparent in the con-

ventional Hubbard model (see Sec. II). The results of the Hartree-Fock study<sup>9</sup> of this spin-flux model are summarized in Sec. III. They suggest that the undoped parent compound is also an AFM Mott insulator. However, unlike the conventional Hubbard model, the one-electron dispersion relations of the AFM mean field in the spin-flux model match those measured experimentally through angle-resolved photoemission for undoped cuprates. A proper description of the highest occupied electronic states (as provided by the spin-flux model), is crucial to considerations of doping. The spin-flux model and the conventional Hubbard model differ dramatically in this regard. At the HF level, the doping holes added to the AFM background of the spin-flux model are trapped in the core of antiferromagnetic spin vortices. This composite object (the meron vortex) is a bosonic charged collective mode of the many-electron system (the total spin of the magnetic vortex is zero). The reversal of the spin-charge connection provides a microscopic basis for non-Fermi-liquid behavior.

A magnetic vortex is strongly attracted to an antivortex. This attraction increases logarithmically with the distance between the vortex cores, and is stronger than the unscreened Coulomb repulsion between the charged meron-vortex cores. In effect, the increase in Coulomb energy between a given pair of holes is more than offset by the lowering in exchange energy between the background electrons as their vortices approach each other from far away. As the intervortex distance increases, more and more spins are rotated out of their AFM background orientation, and the total energy of the system increases. Thus, even at the HF level, the spin-flux model provides a fundamental underpinning for the origin of both non-Fermi-liquid behavior, and strong pairing between the charge carriers.

While providing a good starting point, the Hartree-Fock approximation also has serious shortcomings. For instance, the ground-state wave function in the presence of doping is nonhomogeneous (the static meron vortices of the spin-flux model, or the charged stripes of the conventional Hubbard model, break translational symmetry). Physically, one expects that these charge carriers can move along the planes, resulting in a wave function which preserves the translational symmetry of the original Hamiltonian. The quantum dynamics of the charge carriers also determines whether the doped ground state is really a metal. Charge carriers in the optimally doped cuprates are quite mobile excitations, although their scattering rates are radically different from electrons in a conventional Fermi liquid.

A consistent way of treating the quantum dynamics of the charge carriers is provided by the configuration-interaction (CI) method,<sup>10,3</sup> described in Sec. IV. Here a linear combination of HF wave functions is used in order to restore the various broken symmetries. For instance, in a doped system the CI wave function is chosen to be a linear combination of HF wave functions, with the charge carrier localized at different sites. Certain types of charge carriers can lower their total energy substantially by quantum mechanically hopping from one site to the next. We tested the accuracy of the CI method against the exact solution<sup>11</sup> of the one-dimensional Hubbard model in Ref. 3. In the 1D Hubbard model the CI method describes the quantum dynamics of charged domain wall solitons in the AFM background. By including these

effects as fluctuation corrections to the Hartree-Fock mean-field theory, the CI method provides excellent agreement with the exact Bethe ansatz solution for the ground-state energy of the doped 1D Hubbard chain, over the entire  $U/t$  range. The CI method also leads to a clear demonstration of spin-charge separation in one dimension. The addition of one doping hole to the half-filled antiferromagnetic chain results in the appearance of two different carriers: a charged bosonic domain wall (which carries the charge but no spin) and a neutral spin- $\frac{1}{2}$  domain wall (which carries the spin but no charge). This study<sup>3</sup> demonstrates the effectiveness of the CI method. In this paper we use the CI method to investigate the dynamics of charged meron vortices in the spin-flux model. Throughout this paper we exploit and refer to the analogy between the charge excitations of the 1D Hubbard model and the 2D spin-flux model,<sup>12,13</sup> apparent in the CI approach.<sup>3</sup> The CI results for the spin-flux model (presented in Sec. IV) confirm that the meron vortices are very mobile, suggesting that a collection of such mobile bosonic charge carriers is a non-Fermi-liquid metal. The CI method also allows us to identify the rotational symmetry of the meron-antimeron pair wave function to be *d*-wave for the most stable pairs. An energetically more expensive metastable *s*-wave pairing is also possible. The possibility of spin-charge separation in two dimensions is elucidated. A summary of the results, and their interpretation and conclusions, are provided in Sec. V.

## II. SPIN-FLUX MODEL

The effective 2D Hamiltonian that we use to describe the strongly correlated electrons residing in the  $O(2p)$ - $\text{Cu}(3d_{x^2-y^2})$  orbitals of the isolated  $\text{CuO}_2$  plane is the tight-binding model

$$\mathcal{H} = - \sum_{i,j,\sigma} (t_{ij} c_{i\sigma}^\dagger c_{j\sigma} + \text{H.c.}) + \sum_{i,j} V_{ij} n_i n_j, \quad (1)$$

where  $c_{i\sigma}^\dagger$  creates an electron at site  $i$  with spin  $\sigma$ ,  $t_{ij}$  is the hopping amplitude from site  $j$  to site  $i$  on the square lattice,  $n_i \equiv \sum_{\sigma=1}^2 c_{i\sigma}^\dagger c_{i\sigma}$  is the total number of electrons at site  $i$ , and  $V_{ij}$  is the Coulomb interaction between electrons at sites  $i$  and  $j$ . The dominant terms are the nearest-neighbor hopping  $t_{ij} = t_0$  and the on-site Coulomb repulsion  $V_{ii} = U/2$ . If only these two terms are considered, and we shift the chemical potential by  $U$ , this reduces to the well-known Hubbard model. The neglect of the dynamical consequences of longer-range Coulomb interaction ( $V_{ij} = 0$ , if  $i \neq j$ ), in the Hubbard model, is based the assumption of uniform charge distribution and on the Fermi-liquid theory notion of screening of the effective electron-electron interaction. However, Fermi-liquid theory fails to explain many of the crucial features of the high- $T_c$  cuprates. In our description, we include the nearest-neighbor Coulomb repulsion, which we assume is on the energy scale of  $t$ . This has important dynamical consequences in our model, and cannot simply be absorbed into the Madelung constant. In particular, it leads to the generation of spin flux, to our knowledge, an entirely new type of broken symmetry in the many-electron system, which we show leads naturally to bosonic charge carriers in the form of meron vortices, non-Fermi-liquid behavior, and a strong at-

tractive pairing force between holes in the AFM background. In order to extract the relevant physics from our starting Hamiltonian,

$$\mathcal{H} = -t_0 \sum_{\langle i,j \rangle \sigma} (c_{i\sigma}^\dagger c_{j\sigma} + \text{H.c.}) + U \sum_i n_{i\uparrow} n_{i\downarrow} + V \sum_{\langle i,j \rangle} n_i n_j, \quad (2)$$

we introduce bilinear combination of electron operators  $\Lambda_{ij}^\mu \equiv c_{i\alpha}^\dagger \sigma_{\alpha\beta}^\mu c_{j\beta}$ ,  $\mu=0,1,2$ , and 3, for  $i \neq j$  (summation over multiple indexes is assumed). Here  $\sigma^0$  is the  $2 \times 2$  identity matrix, and  $\vec{\sigma} \equiv (\sigma^1, \sigma^2, \sigma^3)$  are the usual Pauli spin matrices. The notation  $\langle i,j \rangle$  means that sites  $i$  and  $j$  are nearest neighbors. The quantum expectation value  $\langle \cdot \rangle$  of the  $\Lambda_{ij}^\mu$  operators are associated with charge currents ( $\mu=0$ ) and spin currents ( $\mu=1,2$ , and 3). Nonvanishing charge currents lead to appearance of electromagnetic fields, which break the time-reversal symmetry of the Hamiltonian. Experimentally, this does not occur in the cuprates. In the following, we adopt the ansatz that there is no charge current in the ground state  $\Lambda_{ij}^0=0$ , but circulating spin currents may arise and take the form  $\Lambda_{ij}^a = (2t_0/V) i \Delta_{ij} \hat{n}_a$ ,  $a=1,2$ , and 3, where  $|\Delta_{ij}| = \Delta$  for all  $i$  and  $j$ , and  $\hat{n}$  is a unit vector. These spin currents provide a transition state to the uniform spin-flux mean field that we use in this paper. In principle, nonuniform states of spin flux may arise, in which  $|\Delta_{ij}|$  has a nontrivial dependence on  $i$  and  $j$ . One such case was discussed earlier,<sup>8</sup> in which Skyrmion textures in the AFM background carry quantized units of spin flux. In this case  $\Delta_{ij}$  is a dynamical variable. However, for the purpose of this paper, we consider only a uniform, static, mean-field configuration of the spin flux.

Using the Pauli spin-matrix identity  $\frac{1}{2} \sigma_{\alpha\beta}^\mu (\sigma_{\alpha'\beta'}^\mu)^* = \delta_{\alpha\alpha'} \delta_{\beta\beta'}$ , it is possible to rewrite the nearest-neighbor electron-electron interaction terms as  $n_i n_j = 2n_i - \frac{1}{2} \Lambda_{ij}^\mu (\Lambda_{ij}^\mu)^\dagger$ . If we neglect fluctuations in the spin currents, we can use the mean-field factorization  $\Lambda_{ij}^\mu (\Lambda_{ij}^\mu)^\dagger \rightarrow \langle \Lambda_{ij}^\mu \rangle \langle \Lambda_{ij}^\mu \rangle^\dagger + \Lambda_{ij}^\mu \langle \Lambda_{ij}^\mu \rangle^* - \langle \Lambda_{ij}^\mu \rangle \langle \Lambda_{ij}^\mu \rangle^*$ . Thus the quartic nearest-neighbor Coulomb interaction term is reduced to a quadratic term that is added to the hopping term leading to the effective Hamiltonian:

$$\mathcal{H} = -t \sum_{\langle i,j \rangle \alpha\beta} (c_{i\alpha}^\dagger T_{\alpha\beta}^{ij} c_{j\beta} + \text{H.c.}) + U \sum_i n_{i\uparrow} n_{i\downarrow}. \quad (3)$$

Here  $T_{\alpha\beta}^{ij} \equiv (\delta_{\alpha\beta} + i \Delta_{ij} \hat{n} \cdot \vec{\sigma}_{\alpha\beta}) / \sqrt{1 + \Delta^2}$  are spin-dependent SU(2) hopping matrix elements defined by the mean-field theory, and  $t = t_0 \sqrt{1 + \Delta^2}$ . In deriving Eq. (3) we have dropped constant terms which simply change the zero of energy as well as terms proportional to  $\sum_i n_i$  which simply change the chemical potential. It was shown previously<sup>8,14</sup> that the ground state energy of the Hamiltonian of Eq. (3) depends on the SU(2) matrices  $T^{ij}$  only through the plaquette matrix product  $T^{12} T^{23} T^{34} T^{41} \equiv \exp(i \hat{n} \cdot \vec{\sigma} \Phi)$ . Here  $\Phi$  is the spin flux which passes through each plaquette, and  $2\Phi$  is the angle through which the internal coordinate system of the electron rotates as it encircles the plaquette. Since the electron spinor wave function is two valued, there are only two possible choices for  $\Phi$ . If  $\Phi=0$  we can set  $T_{\alpha\beta}^{ij} = \delta_{ij}$ , and

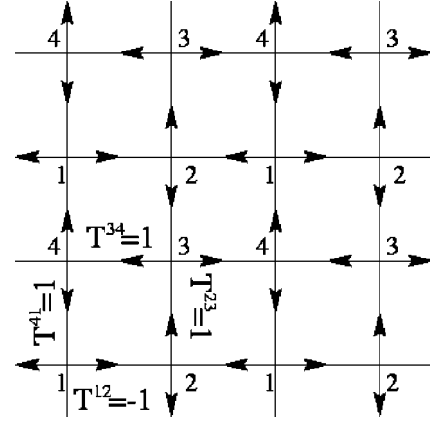


FIG. 1. Choice of the gauge for describing the mean-field spin-flux background. Physical observables depend on the rotation matrices  $T^{ij}$  only through the plaquette matrix product  $T^{12} T^{23} T^{34} T^{41}$ . Shown above is the simplest (spin independent) gauge choice describing a  $2\pi$  rotation of the internal coordinate system of the electron (described by three Euler angles) as it encircles an elementary plaquette. To our knowledge, this is a new form of spontaneous symmetry breaking for a strongly interacting electron system, in which the mean-field Hamiltonian acquires a term with the symmetry of a spin-orbit interaction. This is a dynamical consequence of a nearest-neighbor Coulomb repulsion  $V$  which is comparable to the nearest-neighbor hopping matrix element  $t$ .

Hamiltonian (3) describes conventional ordered magnetic states of the Hubbard model. The other possibility is that a spin flux  $\Phi = \pi$  penetrates each plaquette, leading to  $T^{12} T^{23} T^{34} T^{41} = -1$ . This means that the one-electron wave functions are antisymmetric around each of the plaquettes, i.e., that as an electron encircles a plaquette, its wave function in the internal spin space of Euler angles rotates by  $2\pi$  in response to strong interactions with the other electrons. In effect, the electron performs an internal ‘‘somersault’’ as it traverses a closed path in the  $\text{CuO}_2$  plane.<sup>8</sup> This spin-flux phase is accompanied by an AFM local-moment background (with reduced magnitude relative to the AFM phase of the conventional Hubbard model). In the spin-flux phase, the kinetic-energy term in Eq. (3) exhibits broken symmetry as though a spin-orbit interaction has been added. However, it is distinct from the smaller, conventional spin-orbit effects which give rise to anisotropic corrections to superexchange interactions between localized spins in the AFM.<sup>15</sup> In the presence of charge carriers this mean field is unstable to the proliferation of topological fluctuations (magnetic solitons) which eventually destroy AFM long-range order. In this sense, the analysis which we present below goes beyond simple mean-field theory. The quantum dynamics of these magnetic solitons, described by the configuration-interaction method, corresponds to tunneling effects not contained in the Hartree-Fock approximation. For simplicity, throughout this paper we assume that the mean-field spin flux parameters  $T^{ij}$  are given by the simplest possible choice  $T^{12} = -1, T^{23} = T^{34} = T^{41} = 1$  (see Fig. 1). In order to go beyond a mean-field description of the spin-flux, these matrices may also be treated as dynamical variables. In this paper, we go beyond mean-field theory in describing the antiferromagnetic degrees of freedom, but restrict ourselves to a mean-field model of the spin flux.

### III. HARTREE-FOCK RESULTS FOR THE SPIN-FLUX MODEL

The configuration-interaction method utilizes a linear combination of judiciously chosen Hartree-Fock wave functions.<sup>10,3</sup> In this section, we provide a short review of the relevant Hartree-Fock results for the spin-flux model. A full comparison between the HFA for the spin-flux model and the conventional Hubbard model was published elsewhere.<sup>9</sup>

#### A. Static Hartree-Fock approximation

One of the most widely used approximations for the many-electron problem is the static Hartree-Fock approximation. In this approximation the many-body problem is reduced to one-electron problems in which each electron moves in a self-consistent manner depending on the mean-field potential of the other electrons in the system. While this method is insufficient, in itself, to capture all of the physics of low-dimensional electronic systems with strong correlations, it provides a valuable starting point from which essential fluctuation corrections can be included. In particular, we use the Hartree-Fock method to establish the electronic structure and the static energies of various magnetic soliton structures. In the more general CI variational wave function, the solitons acquire quantum dynamics and describe large amplitude tunneling and fluctuation effects that go beyond mean-field theory.

In the HF approximation, the many-body wave function  $|\Psi\rangle$  is decomposed into a Slater determinant of effective one-electron orbitals. The one-electron orbitals are found from the condition that the total energy of the system is minimized:

$$\delta \frac{\langle \Psi | \mathcal{H} | \Psi \rangle}{\langle \Psi | \Psi \rangle} = 0. \quad (4)$$

In order to approximate the ground state of the spin-flux Hamiltonian [Eq. (3)], we consider a Slater determinant trial wave function of the form

$$|\Psi\rangle = \prod_{p=1}^{N_e} a_p^\dagger |0\rangle, \quad (5)$$

where  $|0\rangle$  is the vacuum state,  $N_e$  is the total number of electrons in the system, and the one-electron states are given by

$$a_n^\dagger = \sum_{i\sigma} \phi_n(i, \sigma) c_{i\sigma}^\dagger. \quad (6)$$

Here the one-particle wave-functions  $\phi_n(i, \sigma)$  form a complete and orthonormal system.

Using wave function (5) in Eq. (4), and minimizing with respect to the one-particle wave functions  $\phi_n(i, \sigma)$ , we obtain the Hartree-Fock eigenequations

$$E_n \phi_n(i, \alpha) = -t \sum_{j \in V_i, \beta} T_{\alpha\beta}^{ij} \phi_n(j, \beta) + U \times \sum_{\beta} \left( \frac{1}{2} \delta_{\alpha\beta} Q(i) - \vec{\sigma}_{\alpha\beta} \vec{S}(i) \right) \phi_n(i, \beta), \quad (7)$$

where  $(\sigma_x, \sigma_y, \sigma_z)$  are the Pauli spin matrices and the charge density

$$Q(i) = \langle \Psi | c_{i\alpha}^\dagger c_{i\alpha} | \Psi \rangle = \sum_{p=1}^{N_e} |\phi_p(i, \alpha)|^2 \quad (8)$$

and spin density

$$\vec{S}(i) = \left\langle \Psi \left| c_{i\alpha}^\dagger \frac{\vec{\sigma}_{\alpha\beta}}{2} c_{i\beta} \right| \Psi \right\rangle = \sum_{p=1}^{N_e} \phi_p^*(i, \alpha) \frac{\vec{\sigma}_{\alpha\beta}}{2} \phi_p(i, \beta) \quad (9)$$

must be computed self-consistently. The notation  $j \in V_i$  appearing in Eq. (7) means that the sum is performed over the sites  $j$  which are nearest neighbors of the site  $i$ . The self-consistent Hartree-Fock equations (7–9) must be satisfied by the occupied orbitals  $p = 1, \dots, N_e$ , but can also be used to compute the empty (hole) orbitals.

The ground-state energy of the system in the HFA is given by

$$E_{GS} = \langle \Psi | \mathcal{H} | \Psi \rangle = \sum_{p=1}^{N_e} E_p - U \sum_i \left( \frac{1}{4} Q(i)^2 - \vec{S}(i)^2 \right), \quad (10)$$

where the single particle energies are obtained from Eq. (7).

The approximation scheme described above is called the unrestricted Hartree-Fock approximation, because we did not impose constraints on the wave function  $|\Psi\rangle$  which would require it to be an eigenfunction of various symmetry operations which commute with Hamiltonian (3). If these symmetries are enforced, the method is called the restricted Hartree-Fock approximation. We use the unrestricted HFA, since it leads to lower energies. The breaking of symmetries in our case implies that electronic correlations are more effectively taken into account.<sup>16</sup> The restoration of these symmetries is deferred until the CI wave function is introduced.

In the undoped (half-filled) case, the self-consistent Hartree-Fock equations can be solved analytically for an infinite system, using plane-wave one-particle wave functions. In the unrestricted Hartree-Fock approach, doping the system leads to the appearance of inhomogeneous solutions, which break the translational invariance. In this case, we solve the unrestricted self-consistent Hartree-Fock equations numerically on a finite lattice. Starting with an initial spin and charge distributions  $\vec{S}(i)$  and  $Q(i)$ , we numerically solve the eigenproblem [Eq. (7)] and find the HF eigenenergies  $E_n$  and wave functions  $\phi_n(i, \alpha)$ . These are used in Eqs. (8) and (9) to calculate the new spin and charge distribution, and the procedure is repeated until self-consistency is reached. Numerically, we define self-consistency by the condition that the largest variation of any of the charge or spin components on any of the sites of the lattice is less than  $10^{-9}$  between successive iterations.

#### B. Undoped ground state

For the undoped system, Hartree-Fock equations (7) for an infinite system are easily solved. In the cuprates, long-range AFM order is experimentally observed. Accordingly, we choose a spin distribution at the site  $i = \vec{e}_x i_x a + \vec{e}_y i_y a$  of

the form  $\vec{S}(i) = (-1)^{(i_x+i_y)} S \vec{e}$ , where  $\vec{e}$  is the unit vector of some arbitrary direction, while the charge distribution is  $Q(i) = 1$ . In the spin-flux phase, it is convenient to choose a square unit cell, in order to simplify the description of the  $T^{ij}$  phase factors. We make the simplest gauge choice compatible with the spin-flux condition for the  $T$  matrices, namely, that  $-T^{12} = T^{23} = T^{34} = T^{41} = 1$  (see Fig. 1). This leads to the reduced square Brillouin zone  $-\pi/2a \leq k_x \leq \pi/2a, -\pi/2a \leq k_y \leq \pi/2a$ . A detailed comparison of the Hartree-Fock energies of the spin-flux phase relative to that of the corresponding non-spin-flux phase were presented elsewhere.<sup>14</sup> Here it was shown that in the range of  $U/t$  and doping relevant to high- $T_c$  superconductors, a uniform spin-flux state has a lower Hartree-Fock energy than a conventional spiral antiferromagnet. From the Hartree-Fock equations we find two electronic bands, characterized by the dispersion relations

$$E_{sf}^{(\pm)}(\vec{k}) = \pm E_{sf}(\vec{k}) = \pm \sqrt{\epsilon_{sf}^2(\vec{k}) + (US)^2}, \quad (11)$$

where each level is fourfold degenerate and  $\epsilon_{sf}(\vec{k}) = -2t \sqrt{[\cos(k_x a)]^2 + [\cos(k_y a)]^2}$  are the noninteracting electron dispersion relations in the presence of spin flux. The HF ground-state energy of the spin-flux AFM background is given by [see Eq. (10)]

$$E_{GS}^{sf} = -4 \sum_{\vec{k}} E_{sf}(\vec{k}) + N^2 U \left( S^2 + \frac{1}{4} \right), \quad (12)$$

where the AFM local-moment amplitude is determined by the self-consistency condition (9):

$$S = \frac{2}{N^2} \sum_{\vec{k}} \frac{US}{E_{sf}(\vec{k})}. \quad (13)$$

At half-filling the valence band ( $E_{sf}^{(-)}(k) < 0$ ) is completely filled, the conduction band ( $E_{sf}^{(+)}(k) > 0$ ) is completely empty, and a Mott-Hubbard gap of magnitude  $2US$  opens between the valence and conduction bands. The ground state of the undoped spin-flux model is an AFM Mott insulator. It is interesting to note that the quasiparticle dispersion relation obtained in the presence of the spin flux [Eq. (11)] closely resembles the dispersion as measured through angle-resolved photoemission spectroscopy (ARPES) in a compound such as  $\text{Sr}_2\text{CuO}_2\text{Cl}_2$  (Ref. 17) (see Fig. 2). There is a large peak centered at  $(\pi/2, \pi/2)$  with an isotropic dispersion relation around it, observed on both the  $(0,0)$  to  $(\pi, \pi)$  and  $(0, \pi)$  to  $(\pi, 0)$  lines. The spin-flux model in the HFA exhibits another smaller peak at  $(0, \pi/2)$  which was observed in more recent experimental data.<sup>18</sup> The quasiparticle dispersion relation of the conventional Hubbard model ( $T^{12} = T^{23} = T^{34} = T^{41} = 1$ ) has a large peak at  $(\pi/2, \pi/2)$  on the  $(0,0)$  to  $(\pi, \pi)$  line (see Fig. 2), but it is perfectly flat on the  $(0, \pi)$  to  $(\pi, 0)$  line (which is part of the large nested Fermi surface of the conventional 2D Hubbard model). Also, it has a large crossing from the upper to the lower band edge on the  $(0,0)$  to  $(0, \pi)$  line. This dispersion relation is very similar to that of the  $t$ - $J$  model (see Ref. 17).

While both the conventional and spin-flux models predict AFM insulators at half-filling (at least at the HF level), the

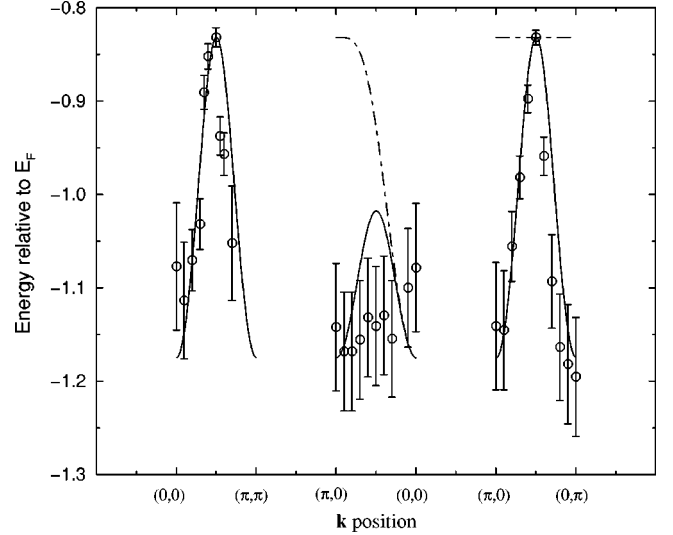


FIG. 2. A comparison between the experimentally determined  $E(\vec{k})$  quasiparticle dispersion relation, from angle-resolved photoemission studies (ARPES), for the insulating  $\text{Sr}_2\text{CuO}_2\text{Cl}_2$  (open circles with error bars) and the HF AFM spin-flux model dispersion relation (full line) and the HF AFM conventional Hubbard model dispersion relation (dash-dotted line). Three directions in  $\vec{k}$  space are shown:  $(0,0)$  to  $(\pi, \pi)$ ,  $(\pi, 0)$  to  $(0,0)$ , and  $(\pi, 0)$  to  $(0, \pi)$ . While the peak in the  $(0,0)$  to  $(\pi, \pi)$  direction is equally well described in both models, the mean-field spin-flux model gives a much better agreement for the  $(\pi, 0)$  to  $(0,0)$  and  $(\pi, 0)$  to  $(0, \pi)$  directions. The fitting corresponds to  $U = 2.01$  eV and  $t = 0.29$  eV for the spin-flux phase, and  $U = 1.98$  eV and  $t = 0.21$  eV in the conventional phase. The experimental results are the ARPES results of Ref. 17.

spin-flux model also provides a much better agreement with the dispersion relations, as measured by ARPES. As in the 1D case,<sup>3</sup> the effect of doping is the appearance of discrete levels deep inside the Mott-Hubbard gap. These levels are drawn into the gap from the top (bottom) of the undoped valence (conduction) bands. Accordingly, the type of excitations created by doping depends strongly on the topology of the electronic structure near the band edges.

### C. Charged solitons in the doped insulator: Spin bag and meron vortex

#### 1. Spin bag

If we introduce just one hole in the plane, the self-consistent HFA solution is a conventional spin polaron or “spin bag” [see Fig. 3(a)]. This type of excitation is the 2D analog of the 1D spin polaron.<sup>3</sup> The doping hole is localized around a particular site, leading to the appearance of a small ferromagnetic core around that site. The spin and charge distribution at the other sites are only slightly affected. In fact, the localization length of the charge depends on  $U/t$ , and becomes very large as  $US \rightarrow 0$ , since in this limit the Mott-Hubbard gap closes. For intermediate and large  $U/t$ , the doping hole is almost completely localized on the five sites of the ferromagnetic core.

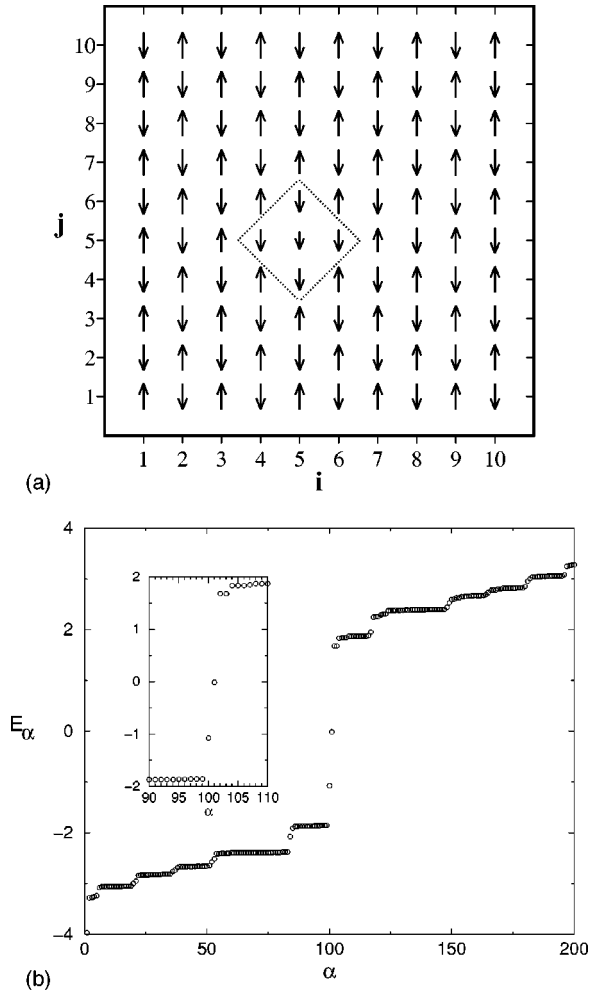


FIG. 3. (a) Self-consistent spin distribution of a  $10 \times 10$  lattice with a spin bag centered at (5,5). The spin bag has a small ferromagnetic core, and the magnetic order is only locally affected. (b) Electronic spectrum of a spin bag on a  $10 \times 10$  lattice, for  $U/t=5$  in the spin-flux model. Eigenenergies  $E_\alpha$  are plotted as a function of  $\alpha=1,200(=2N^2)$ . Only the first  $N^2-1=99$  states are occupied. There are two empty bound discrete levels deep in the Mott-Hubbard gap ( $\alpha=100$  and  $101$ ), one of which comes from the valence band of the undoped AFM compound (see the inset). There is also an occupied discrete level below the valence band ( $\alpha=1$ ). The valence band is spin paired, since it has an even number of levels. Thus the total spin of the spin bag comes from the discrete occupied level below the valence band. The spin bag is a charged, spin- $\frac{1}{2}$  fermion.

The spin bag is a charged fermion, as can be seen by direct inspection of its charge and spin distributions. This is also confirmed by its electronic structure [see Fig. 3(b)]. The spin bag is accompanied by a total of four discrete levels that split off from the valence band and conduction band. Two localized electronic states emanate from the top and bottom of the valence band. Two more such localized levels emanate from the top and bottom of the conduction band. Of these four discrete levels only the state below the valence band is occupied. The occupation of this low-lying bound level by a spin- $\frac{1}{2}$  electron ensures that the overall spin-bag configuration is a charged fermion. The occupied continuum states of the valence band are spin paired, and do not contribute to the

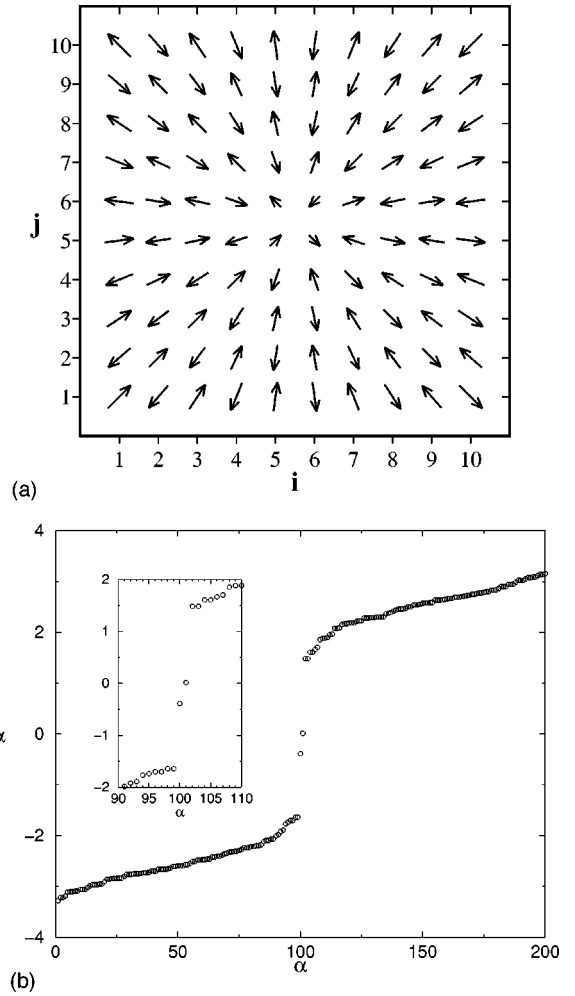


FIG. 4. (a) Self-consistent spin distribution of a  $10 \times 10$  lattice with a meron vortex in the spin-flux phase. The core of the meron is localized in the center of a plaquette, in the spin-flux phase (in the conventional phase, the core of the meron vortex is localized at a site). This excitation has a topological winding number 1, since the spins on either sublattice rotate by  $2\pi$  on any curve surrounding the core. The magnitude of the staggered magnetic moments is slightly diminished near the vortex core, but is equal to that of the undoped AFM background far from the core. (b) Electronic spectrum of a meron vortex on a  $10 \times 10$  lattice, for  $U/t=5$ , in the presence of the spin flux. Eigenenergies  $E_\alpha$  are plotted as a function of  $\alpha=1,200(=2N^2)$ . Only the first  $N^2-1=99$  states are occupied (the valence band). There are two discrete empty levels deep in the Mott-Hubbard gap, one of which ( $\alpha=100$ ) comes from the valence band of the undoped AFM parent. Merons must be created in vortex-antivortex pairs (for topological reasons). Each pair removes two levels from the undoped AFM valence band. Thus the valence band remains spin paired, and the total spin of this excitation is zero. This meron is a spinless, charged, bosonic collective excitation of the doped antiferromagnet.

overall spin of this collective mode. Thus the 2D spin bag is indeed the analog of the 1D spin polaron.<sup>3</sup>

## 2. Meron vortex

The 2D analog of the 1D charged domain wall is the meron vortex (see Fig. 4). Like the 1D domain wall, the meron vortex (antivortex) is also a topological excitation,

characterized by a topological winding number  $+1$  ( $-1$ ) [the spins on each sublattice rotate by  $2\pi$  ( $-2\pi$ ) on any closed contour surrounding the center of the meron vortex (antivortex)]. As such, a single meron vortex cannot be created in an extended AFM background with cyclic boundary conditions by the introduction of a single hole [just as a single isolated charged domain wall cannot be created on an AFM (even) chain with cyclic boundary conditions, by the introduction of a single hole]. From a topological point of view, this is so because the AFM background has a winding number 0, and the winding number must be conserved, unless topological excitations migrate over the boundary into the considered region. However, excitations can be created in pairs of total topological number 0. In the 1D case, this means the creation of pairs of domain walls, while in two dimensions this means the creation of vortex-antivortex pairs.

From Figs. 4(a) and 4(b), we can see that the total spin of the meron vortex (antivortex) is zero, while it carries the doping charge trapped in the vortex core. Moreover, from its electronic spectrum [Fig. 4(b)], we can see that only the extended states of the valence band are occupied. They are the only ones contributing to the total spin. Since only one state is drawn from the valence band into the gap, to become a discrete bound level, it appears that an odd (unpaired) number of states remains in the valence band. However, one must remember that, for topological reasons, merons must appear in vortex-antivortex pairs. Therefore, the valence band has an even number of (paired) levels, and the total spin is zero. This argument for the bosonic character of the meron vortex is identical to that for the charged domain wall in polyacetylene.<sup>13,19,20</sup> This shows that the net spin of a charged meron plus a charged antimeron is always zero. The fact that the individual meron and antimeron are spinless is evident from the fact that neither of them have an occupied localized electronic state. This is very different from the spin bag, which acquired its fermionic character through an occupied discrete level below the valence band.

Unlike in the 1D case,<sup>3</sup> we cannot directly compare the excitation energy of the spin bag with the excitation energy of the meron vortex. The reason for this is that the excitation energy of the latter increases logarithmically with the size of the sample, and therefore an isolated meron vortex is always energetically more expensive than a spin bag. However, topology requires that merons and antimerons are created in pairs. The excitation energy of such a meron-antimeron pair is finite, allowing a meaningful comparison between excitation energies of a pair of spin bags and a meron-antimeron pair.

### 3. Meron-antimeron pair

In Figs. 5(a) and 5(b) we show the self-consistent spin and charge distributions for the lowest-energy self-consistent HF configuration found when we add two holes to the AFM background, in the spin-flux model, for  $U/t=5$ . This configuration consists of a meron and an antimeron centered on second-nearest-neighbor sites. As a result of interactions, the cores of the vortices are somewhat distorted. If the vortices were uncharged, vortex-antivortex pair annihilation would be possible. However, for charged vortices, the fermionic nature

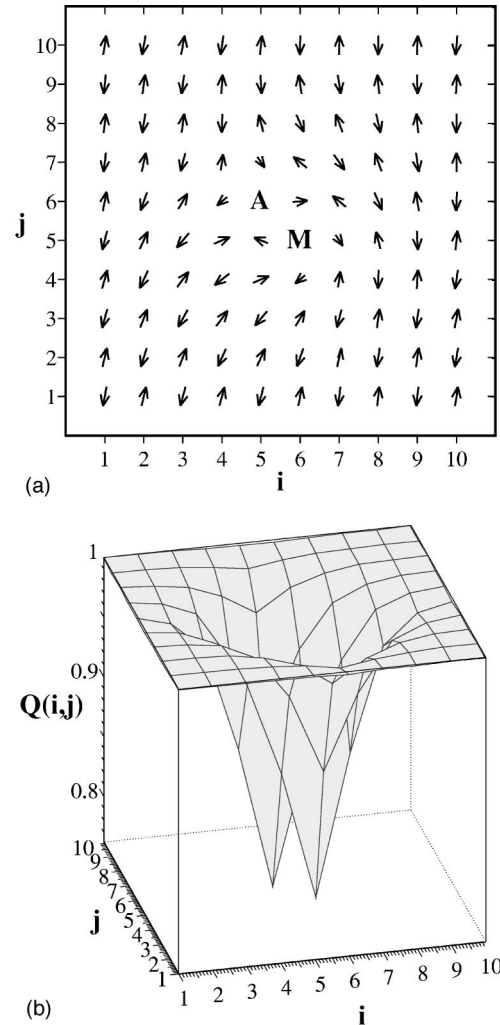


FIG. 5. (a) Self-consistent spin distribution for a tightly bound meron-antimeron pair. The meron ( $M$ ) and antimeron ( $A$ ) are localized on neighboring sites. The total winding number of the pair is zero. The magnetic AFM order is disturbed only on the region where the vortices are localized. The attraction between holes is of topological nature, and on a long length scale is stronger than the unscreened Coulomb repulsion between charges. (b) Self-consistent charge distribution for a tightly bound meron-antimeron pair. The doping charge is mostly localized on the two plaquettes containing the meron and antimeron cores. The two holes localized in the vortex cores are responsible for the fact that the meron-antimeron pair does not collapse (due to Fermi statistics, it is impossible to have two holes at the same site).

of the underlying electrons prevents two holes from being localized at the same site, in spite of the bosonic character of the collective excitation.

A very interesting feature of this configuration is the strong topological attraction between the vortex and the antivortex. The closer the two cores are to each other, the smaller the region is in which the spins are rotated out of their background AFM orientation by the vortices, and therefore the smaller the excitation energy of the pair is. Since the holes are localized in the cores of the vortices, this topological attraction between vortices is an effective attraction between holes in the purely repulsive 2D electron system. This effect is unique to the spin-flux phase. In the conventional

Hubbard model, vortices are not stable excitations. In the spin-flux phase, the vortex-antivortex attraction increases as the logarithm of the distance between the cores. Therefore, the pair of vortices remains bound even in the presence of Coulomb repulsion between the charged cores. Eventually, at long distances the charge carriers can overcome their logarithmic attraction by decaying into a pair of spin bags. For this to occur the logarithmic exchange energy cost would need to exceed the kinetic energy of delocalization gained by the moving meron-antimeron pair. In the doping range relevant to superconductivity, this would only occur if the meron-antimeron pair were pulled further apart than the (doping-dependent) antiferromagnetic correlation length. As a result, the decay of a meron-antimeron pair into a pair of spin bags is not realized in practice. The logarithmic attractive force provides a compelling scenario for the existence of strongly bound preformed pairs in the underdoped regime.

There is another possible self-consistent state for the system with two holes, consisting of two spin bags far from each other (such that their localized wave functions do not overlap). The excitation energy of such a pair of spin bags is simply twice the excitation energy of a single spin bag. When this excitation energy is compared to the excitation energy of the tightly bound meron-antimeron pair, we find that it is higher by  $0.15t$  (for  $U/t=5$ ). In fact, for  $U/t < 8$  the HFA predicts that the meron-antimeron pair is the low-energy charged excitation, while for  $U/t > 8$ , the spin bag is the low-energy charge carrier. This is analogous with the situation in one dimension, where the spin bag was predicted to be the low-energy excitation for  $U/t > 6.5$ , in the HFA.<sup>3</sup> As in one dimension, however, we expect that this conclusion will be drastically modified once the charged solitons are allowed to move along the planes and the lowering of kinetic energy through translations is also taken into consideration.

We complete this review of the HF results by pointing out that the strong analogy between the 1D Hubbard model and the 2D spin-flux model is due to the similarity between the electronic structures at zero doping. As seen from Fig. 2, the 2D spin-flux model has isotropic dispersion relations about the  $(\pi/2, \pi/2)$  point. This acts as a Fermi point for the non-interacting system as it does in the 1D system. The two empty discrete levels drawn deep inside the Mott-Hubbard gap in the presence of the meron-vortex split from the  $(\pi/2, \pi/2)$  peaks of the electron dispersion relation. The different topology of the large nested Fermi surface of the conventional Hubbard model leads to an instability of the meron-antimeron pair. In fact, in the conventional Hubbard model doping holes assemble in charged stripes, as opposed to the liquid of meron-antimeron pairs, which is the low-energy state of the doped spin-flux model.

#### IV. CONFIGURATION INTERACTION METHOD RESULTS FOR THE 2D SYSTEM

##### A. Configuration interaction method

The essence of the CI method is that the ground-state wave function, for a system with  $N_e$  electrons, is not represented by just a single  $N_e \times N_e$  Slater determinant (as in the

HFA), but a judiciously chosen linear combination of such Slater determinants.<sup>10</sup> Given the fact that the set of all possible Slater determinants (with all possible occupation numbers) generated from a complete set of one-electron orbitals constitute a complete basis of the  $N_e$ -particle Hilbert space, our aim is to pick out a subset of Slater determinants which captures the essential physics of the exact solution.

Consider the CI ground-state wave function given by

$$|\Psi\rangle = \sum_{i=1}^N \alpha_i |\Psi_i\rangle, \quad (14)$$

where each  $|\Psi_i\rangle$  is a distinct  $N_e \times N_e$  Slater determinant, and the coefficients  $\alpha_i$  are chosen to satisfy the minimization principle

$$\frac{\delta}{\delta \alpha_i} \left( \frac{\langle \Psi | \mathcal{H} | \Psi \rangle}{\langle \Psi | \Psi \rangle} \right) = 0, \quad i=1, N. \quad (15)$$

This leads to the system of CI equations

$$\sum_{j=1}^N \mathcal{H}_{ij} \alpha_j = E \sum_{j=1}^N O_{ij} \alpha_j, \quad i=1, N, \quad (16)$$

where  $E = \langle \Psi | \mathcal{H} | \Psi \rangle / \langle \Psi | \Psi \rangle$  is the energy of the system in the  $|\Psi\rangle$  state,  $\mathcal{H}_{ij} = \langle \Psi_i | \mathcal{H} | \Psi_j \rangle$  are the matrix elements of the Hamiltonian in the basis of Slater determinants  $\{|\Psi_i\rangle, i=1, N\}$ , and  $O_{ij} = \langle \Psi_i | \Psi_j \rangle$  are the overlap matrix elements of the Slater determinants (which are not necessarily orthogonal). The CI solution is easily found by solving the linear system of equations (16), once the basis of Slater determinants  $\{|\Psi_i\rangle, i=1, N\}$  is chosen. If we denote by  $\phi_p^{(n)}(i, \sigma)$  the  $p=1, \dots, N_e$  one-electron occupied orbitals of the Slater determinant  $|\Psi_n\rangle$ , these matrix elements are given by

$$O_{nm} = \begin{bmatrix} \beta_{1,1}^{nm} & \dots & \beta_{1,N_e}^{nm} \\ \vdots & & \vdots \\ \beta_{N_e,1}^{nm} & \dots & \beta_{N_e,N_e}^{nm} \end{bmatrix}. \quad (17)$$

The matrix elements of Hamiltonian (3) can be written as

$$\mathcal{H}_{nm} = -t \cdot \mathcal{T}_{nm} + U \sum_i \mathcal{V}_{nm}(i), \quad (18)$$

where the expectation values of the hopping and on-site interaction terms are:

$$\mathcal{T}_{nm} = \sum_{p=1}^{N_e} \begin{vmatrix} \beta_{1,1}^{nm} & \cdots & t_{1,p}^{nm} & \cdots & \beta_{1,N_e}^{nm} \\ \vdots & & \vdots & & \vdots \\ \beta_{N_e,1}^{nm} & \cdots & t_{N_e,p}^{nm} & \cdots & \beta_{N_e,N_e}^{nm} \end{vmatrix}$$

and

$$\mathcal{V}_{nm}(i) = \sum_{p_1 \neq p_2} \begin{vmatrix} \beta_{1,1}^{nm} & \cdots & u_{1,p_1}^{nm}(i) & \cdots & d_{1,p_2}^{nm}(i) & \cdots & \beta_{1,N_e}^{nm} \\ \vdots & & \vdots & & \vdots & & \vdots \\ \beta_{N_e,1}^{nm} & \cdots & u_{N_e,p_1}^{nm}(i) & \cdots & d_{N_e,p_2}^{nm}(i) & \cdots & \beta_{N_e,N_e}^{nm} \end{vmatrix}.$$

Here

$$\beta_{ph}^{nm} = \sum_{i\sigma} \phi_h^{(n)*}(i, \sigma) \phi_p^{(m)}(i, \sigma),$$

$$t_{p_1, p_2}^{nm} = \sum_{\substack{\langle i, j \rangle \\ \alpha\beta}} [\phi_{p_1}^{(n)*}(i, \alpha) T_{\alpha\beta}^{ij} \phi_{p_2}^{(m)}(j, \beta) + \text{H.c.}],$$

$$u_{p_1, p_2}^{nm}(i) = \phi_{p_2}^{(n)*}(i \uparrow) \phi_{p_1}^{(m)}(i \uparrow),$$

and

$$d_{p_1, p_2}^{nm}(i) = \phi_{p_2}^{(n)*}(i \downarrow) \phi_{p_1}^{(m)}(i \downarrow).$$

We now consider the specific choice of the Slater determinant basis  $\{|\Psi_i\rangle, i=1, \dots, N\}$ . Strictly speaking, one may choose an optimized basis of Slater determinants from the general variational principle:

$$\frac{\delta}{\delta \phi_p^{(n)}(i, \sigma)} \left( \frac{\langle \Psi | \mathcal{H} | \Psi \rangle}{\langle \Psi | \Psi \rangle} \right) = 0, \quad n=1, N, \quad p=1, N_e. \quad (19)$$

However, implementation of this full trial-function minimization scheme (also known as a multireference self-consistent mean-field approach<sup>16</sup>) is numerically cumbersome even for medium-sized systems. Instead, we select the Slater determinant basis  $\{|\Psi_i\rangle, i=1, N\}$  from the set of broken symmetry, unrestricted Hartree-Fock wave functions [Eq. (5)], their symmetry-related partners, and their excitations. Clearly, Eq. (5) satisfies Eq. (19) by itself, provided that the  $\alpha$  coefficients corresponding to the other Slater determinants in Eq. (14) are set to zero [see Eq. (4)]. Since this unrestricted HF wave function is not translationally invariant (the doping hole is always localized somewhere on the lattice), we can restore the translational invariance of the CI ground-state wave function by also including in the basis of Slater determinants all the possible lattice translations of this unrestricted HF wave function. Furthermore, if the self-consistent configuration is not rotationally invariant (e.g., a meron-antimeron pair), all possible rotations must be performed as well. By rotation we mean changing the relative position of the meron and antimeron while keeping their center of mass fixed.

Clearly, all the translated HF Slater determinants lead to the same HF ground-state energy  $\langle \Psi_n | \mathcal{H} | \Psi_n \rangle = E_{GS}$  as de-

finied by Eq. (10). The CI method lifts the degeneracy between states with the hole-induced configuration localized at different sites [see Eq. (16)], thereby restoring translational invariance. We may identify the lowering in the total energy due to the lifting of this degeneracy as quantum-mechanical kinetic energy of deconfinement which the doping-induced configuration saves through hopping along the lattice. In addition, quantum fluctuations in the internal structure of a magnetic soliton can be incorporated by including the lowest-order excited-state configurations of the static Hartree-Fock energy spectrum. Such wave functions are given by  $a_p^\dagger a_h |\Psi\rangle$ , where  $p > N_e$  labels an excited particle state and  $h \leq N_e$  labels the hole which is left behind [see Eq. (5)]. Once again, all possible translations (and nontrivial rotations) of these ‘‘excited’’ configurations must be included in the full CI wave function. These additions can describe changes in the ‘‘shape’’ of the soliton as it undergoes quantum-mechanical motion along the plane. However, such particle-hole-excited configurations have much higher energies than the ground-state HF configurations. This is due to the fact that the valence band is filled at all dopings, so particle-hole excitations involve at least the excitation of an electron from the valence band to one of the empty midgap electronic levels trapped in the vortex cores, raising the total energy by roughly  $U/2$ . As a result, these much higher-energy states do not contribute significantly to the CI ground state, but rather to states higher up on the dispersion curve (roughly from  $U/2$  above the CI ground-state energy). In this paper we concentrate on the CI ground states. Accordingly, we do not include such high-energy particle-hole-excited states in the set of Slater determinants  $\{|\Psi_i\rangle, i=1, \dots, N\}$ .

The CI method was described in more detail in Ref. 3, where it was used to study the 1D Hubbard chain in order to gauge its accuracy by comparing its results with the exact Bethe ansatz solution. We showed that the CI method recaptures the essential physical features of the exact solution of the 1D Hubbard chain, such as spin-charge separation, as well as leading to a remarkable agreement of ground-state energies of doped chains for all values of  $U/t$ . The main difference between the 1D and 2D cases is the computation time required. The computation time for one matrix element  $\mathcal{H}_{nm}$  scales roughly like  $N^9$ , where  $N$  is the number of sites. The number of configurations included in the CI set scales as  $N!/N_s!(N-N_s)!$  when  $N_s$  solitons are present. For both an  $N$ -site chain and an  $N \times N$  lattice, the HF ‘‘bulk’’ limit is

reached for  $N \geq 10$ . In the 1D case<sup>3</sup> we used chains with  $N = 10-25$ , and numerical calculations can be easily performed. However, in two dimensions the smallest acceptable system has 100 sites, leading to an enormous increase in the computation time. Nevertheless, our sample of results in two dimensions suggests a simple and clear physical picture which we describe below.

### B. Spin-bag dissociation: Spin-charge separation precursor effects in two dimensions

The charged spin bag carries a spin of  $1/2$ . Let  $|\Psi_+\rangle, |\Psi_-\rangle$  be the HF determinants for a spin bag centered at any two nearest-neighbor sites, respectively, and let  $\hat{S}_z = \sum_i \hat{S}_z(i) = \frac{1}{2} \sum_{i,\sigma} \sigma c_{i\sigma}^\dagger c_{i\sigma}$  be the total spin operator in the  $z$  direction. Then  $\hat{S}_z |\Psi_+\rangle = \frac{1}{2} |\Psi_+\rangle$  while  $\hat{S}_z |\Psi_-\rangle = -\frac{1}{2} |\Psi_-\rangle$  (or vice versa), since moving the center of the spin bag by one site leads to a flip of its total spin [see Fig. 3(a)]. Consequently,  $\langle \Psi_- | \Psi_+ \rangle = 0$ . Since the Hubbard Hamiltonian commutes with  $\hat{S}_z$ , it follows that  $\langle \Psi_- | \mathcal{H} | \Psi_+ \rangle = 0$ . From the CI equation (16) we conclude that there is no mixing between states with different total spins. As a result, it is enough to include in the CI set only those configurations with the spin bag localized on the same magnetic sublattice. Let us denote by  $|\Psi_{(0,0)}\rangle$  the initial static Hartree-Fock configuration, and by  $|\Psi_{(n,m)}\rangle$  the configuration obtained through its translation by  $n$  sites in the  $x$  direction and  $m$  sites in the  $y$  direction (cyclic boundary conditions are imposed). The condition that only configurations on the same sublattice are included means that  $n+m$  must be an even number, and the cyclic boundary conditions mean that  $0 \leq n \leq N-1, 0 \leq m \leq N-1$ , for a  $N \times N$  lattice. As explained in detail in the 1D analysis,<sup>3</sup> mixing configurations with the charged spin bag localized at different sites and then subtracting out the contribution of the undoped AFM background allows us to calculate the dispersion band of the spin bag itself:

$$E_{sb}(\vec{k}) = E(\vec{k}, N) - N^2 e_{GS}. \quad (20)$$

Here the total energy of the lattice with the spin bag,

$$E(\vec{k}, N) = \frac{\langle \Psi_{\vec{k}} | \mathcal{H} | \Psi_{\vec{k}} \rangle}{\langle \Psi_{\vec{k}} | \Psi_{\vec{k}} \rangle},$$

and the CI wave function,

$$|\Psi_{\vec{k}}\rangle = \sum_{(n,m)} \exp[i(k_x n + k_y m) a] |\Psi_{(n,m)}\rangle,$$

are the solutions of the CI equations (16). The finite size of the lattice and cyclic boundary conditions restricts the calculation to  $\vec{k}$  points of the form  $\vec{k} = 2\pi/N a (\alpha \vec{e}_x + \beta \vec{e}_y)$ , where  $(\alpha, \beta)$  is any pair of integer numbers. As usual, only  $\vec{k}$  points inside the first Brillouin zone need to be considered.

An analysis of the dependence of the spin-bag dispersion relation  $E_{sb}(\vec{k})$  on the size  $N \times N$  of the lattice is shown in Fig. 6, for the conventional Hubbard model (upper panel) and the spin-flux model (lower panel), and  $U/t = 5$ . We used  $6 \times 6$ ,  $8 \times 8$ ,  $10 \times 10$  and (only for the spin-flux model)  $12 \times 12$  lattices. The dispersion relation is plotted along lines of high symmetry of the full Brillouin zone. For comparison,

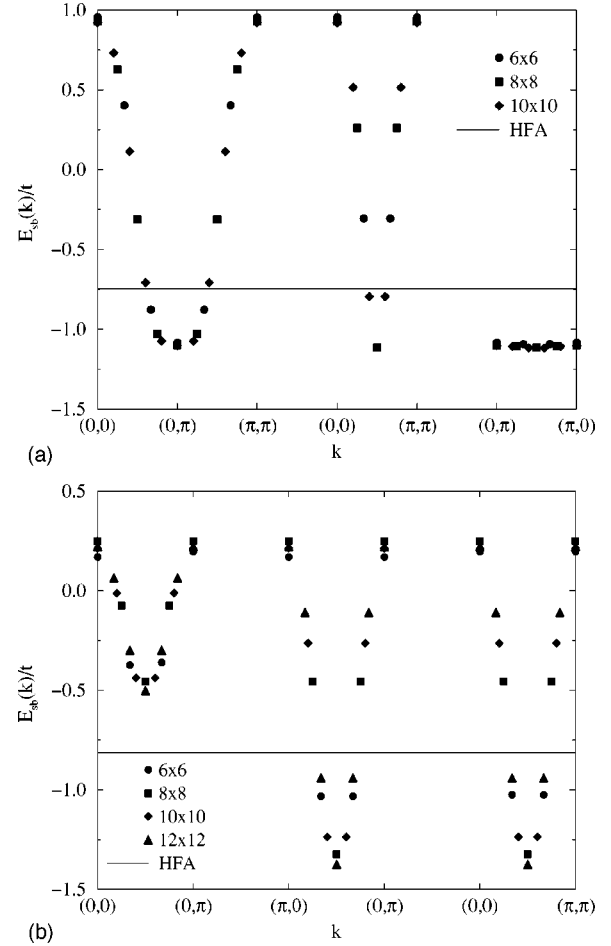


FIG. 6. Dispersion relation of the charged spin bag  $E_{sb}(\vec{k})$  (in units of  $t$ ) plotted along lines of high symmetry in the Brillouin zone. The upper plot shows the dispersion band of the spin bag in the conventional model, while the lower one shows the dispersion band of the spin bag in the spin-flux model.  $U/t = 5$  in both cases. Circles, squares, diamonds, and triangles show the results obtained from CI analysis of  $6 \times 6$ ,  $8 \times 8$ ,  $10 \times 10$ , and  $12 \times 12$  lattices. We conclude that the results are already almost converged, even for such small lattices. The full lines show the excitation energy of the spin bag at the static HF level.

we also show the excitation energy  $E_{sb}^{HF}$  obtained in the static HFA as a full line. For both models, we see that the spin-bag dispersion band is almost converged, even though we used quite small lattices. The convergence is somewhat slower in the spin-flux case, as seen most clearly at the  $(0,0)$  point. Although the values obtained from the four lattices all differ at  $(0,0)$ , the extremum values correspond to the  $6 \times 6$  and  $8 \times 8$  lattices, while the values for the  $10 \times 10$  and  $12 \times 12$  lattices are indistinguishable. We conclude that the fit [Eq. (20)] is legitimate.

From Fig. 6 we also see that the dispersion relations for the spin bag in the two different models are very different. The dispersion relations over the full 2D Brillouin zone are shown in Fig. 7, and they are seen to mimic the electronic dispersion relation of the underlying undoped AFM background, shown in Fig. 2. This is consistent with the quasiparticle nature of this charged spin- $\frac{1}{2}$  spin bag. In the conventional Hubbard model, the undoped AFM background has a large nested Fermi surface along the  $(0,\pi)$  to  $(\pi,0)$

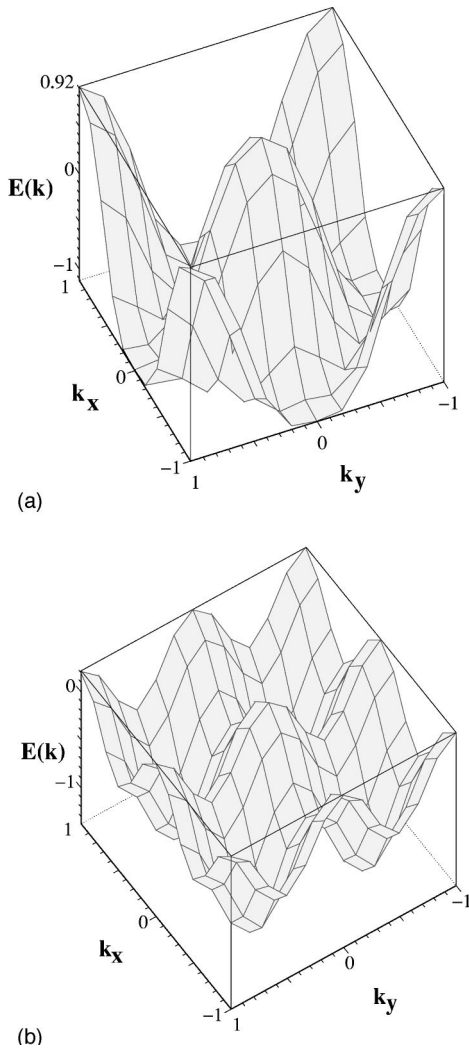


FIG. 7. Dispersion band of the spin bag in the conventional model (upper panel) and the spin-flux model (lower panel), for  $U/t=5$ . We show the full 2D Brillouin zone ( $k$  is measured in units of  $\pi/a$ ). The spin-bag dispersion relations have the same symmetry as the dispersion relations of the underlying undoped AFM background, shown in Fig. 2. While the  $(\pi/2a, \pi/2a)$  point corresponds to the minimum excitation energy of the spin-flux spin bag, in the conventional model all points along the  $(0, \pi)$  to  $(\pi, 0)$  direction have almost the same energy.

line, and it is exactly along this line that the spin bag dispersion band has a minimum. Similarly, the lowest energy of the spin bag of the spin-flux model is at  $(\pi/2, \pi/2)$ , corresponding to the Fermi points of the underlying undoped spin-flux AFM background.

The extra kinetic energy  $E_{sb}(\pi/2, \pi/2) - E_{sb}^{HF}$  saved by the spin bag through quantum hopping is  $0.37t$  in the conventional model and  $0.56t$  in the spin-flux model (for  $U/t=5$ ). Since the spin bag is confined to one magnetic sublattice, it must tunnel two lattice constants to the next allowed site. Consequently, the energy gained through hopping (of order  $t^2/U$ ) is small. This is displayed, for the spin bag of the spin flux model, in Fig. 8, where we plot the lowering in kinetic energy of the deconfined spin bag  $E_{sb}(\pi/2, \pi/2) - E_{sb}^{HF}$  as a function of  $t/U$ . A similar dependence for the spin bag of the conventional Hubbard model was presented

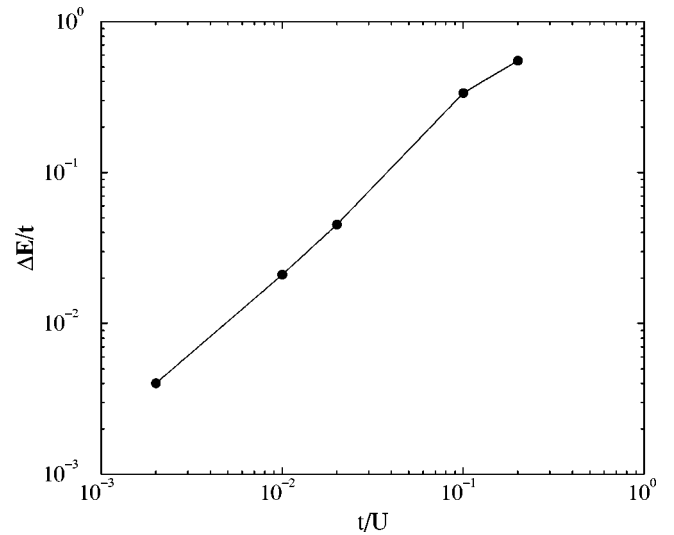


FIG. 8. The extra kinetic energy (in units of  $t$ ) gained by the spin bag  $\Delta E = E_{sb}(\pi/2, \pi/2) - E_{sb}^{HF}$  (circles) as a function of  $t/U$ . The log-log graph clearly shows the linear dependence. This is expected, since the spin bag must tunnel two sites to the next allowed position. This is a second-order hopping process, and therefore this charged excitation is rather immobile.

elsewhere.<sup>10</sup> As in the 1D case, we conclude that the spin bag in two dimensions is a rather immobile quasiparticlelike excitation.

In the 1D model it is energetically favorable for the immobile spin bag to decay into a charged bosonic domain wall and a neutral fermionic domain wall, resulting in spin-charge separation.<sup>3</sup> The analog of the 1D charged bosonic domain wall is the 2D charged bosonic meron vortex of the spin-flux model. If the spin bag decays into a charged meron-vortex, a magnetic antivortex must also be created for topological reasons. Unlike the pair of domain walls in the 1D case, the vortex-antivortex pair is tightly bound by a topological binding potential that increases as the logarithm of the vortex-antivortex separation. Therefore, we expect that the doping charge is shared between the two magnetic vortices. One technical problem for testing this hypothesis is that such a configuration (a vortex-antivortex pair sharing one doping hole) is not self-consistent at the static Hartree-Fock level. In the static approximation we require two doping holes to stabilize two vortex cores and create a meron-antimeron pair. We can, however, construct a trial wave function to describe the singly charged vortex-antivortex pair, by adding one electron in the first empty state of the self-consistent doubly charged meron-antimeron configuration. The first empty levels of the meron-antimeron pair are the localized levels bound in the vortex cores, two for each vortex [see Fig. 4(b)]. Because of degeneracy between the two lower discrete levels of the pair, we have in fact two distinct trial wave functions, obtained by adding one electron in either of these two lower localized gap electronic states of a self-consistent meron-antimeron pair. These wave functions are not invariant to rotations (see Fig. 5). Therefore, in the CI set of Slater determinants we must include the configurations obtained through  $\pi/2$  rotations of the vortex-antivortex pair about its fixed center of mass in addition to translated configurations. As a result, we have a total of  $8N^2$  configurations describing

the singly charged vortex-antivortex pair localized at all possible sites with all possible orientations about the center of mass.

We performed this CI analysis for a  $10 \times 10$  lattice and  $U/t=5$ . The HF energy of a simple static spin bag is  $-0.82t$  (measured with respect to the HF energy of the undoped AFM background, equal to  $-76.76t$ ). The energy of the static singly charged vortex-antivortex pair is  $-0.23t$ . Thus we see that because this singly charged pair trial wave function is not self-consistent, in the static case this configuration is energetically much more costly than the self-consistent spin-bag configuration. However, if we allow for quantum motion of these configurations, the situation changes dramatically. Performing a CI analysis for the set of all possible translated spin-bag configurations, we find that the energy of the spin bag is lowered to  $-1.24t$ . Performing a CI analysis for the set of all translated and rotated singly charged vortex-antivortex pairs, we find that this configuration's energy is lowered to  $-2.18t$ . This shows that the vortex-antivortex pair has lowered its translational and rotational kinetic energy by almost  $2t$ , thereby becoming a low-energy charge carrier. This large number is not surprising since, unlike the spin bag, the vortex-antivortex pair is not constrained to motion on one magnetic sublattice. As a result, such configurations lower their kinetic energy by an amount on the scale of  $t$ , as opposed to  $t^2/U$  for the spin-bag configuration. For larger  $U/t$  values this effect is even more pronounced.

We conclude that these results strongly support the hypothesis of spin-bag dissociation into a much more mobile singly charged vortex-antivortex pair, analogous to the 1D spin-bag dissociation into a pair of a charged bosonic domain wall and a neutral fermionic domain wall.<sup>3</sup> Unlike in the 1D case, however, we do not have distinct charge and spin carriers for the composite excitation. Instead, the spin and charge are shared equally between the vortex and antivortex. If, on the other hand, there was a mechanism whereby the vortices became unbound, complete spin-charge separation could occur, in which one vortex traps the hole (and is therefore a charged meron) and the other vortex carries the spin, in a lotus-flower<sup>12,13</sup> (or undoped magnetic meron) configurations. At very low doping, the strong vortex-antivortex topological attraction binds the spin and charge together. This is different from the 1D case, where the absence of long-range interactions between the domain walls allow for a complete spin-charge separation even if there is just one doping hole on the chain, and even at zero temperature.

This scenario opens an avenue for research into how the system evolves with doping. If each hole is dressed into a singly charged vortex-antivortex pair, when two such pairs overlap it is possible that both doping charges move to the same pair, creating a more stable meron-antimeron pair of charged bosons. Such preformed charge pairs may condense into a superconducting state at low temperatures. The other uncharged vortex-antivortex pair may either collapse and disappear (this is likely to happen at low temperatures) or remain as a magnetic excitation of the system (at higher temperatures), mediating the destruction of the long-range AFM order, the renormalization of the spin-wave spectrum, and

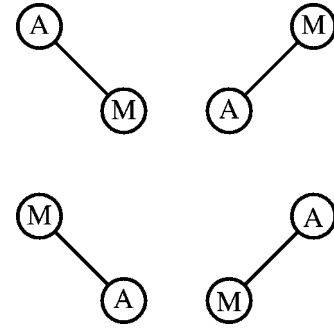


FIG. 9. Schematic representation of the four different meron-antimeron pair configurations obtained through  $\pi/2$  rotation about their fixed center of mass. The upper-left picture is a schematic representation of the self-consistent meron-antimeron pair shown in Fig. 5.

the opening of the spin pseudogap. Thus, at higher doping we effectively see spin-charge separation even in a two-dimensional system.

### C. *D*-wave pairing of charge carriers

From the static HF analysis we found that the most stable static self-consistent configuration with two doping holes added to the AFM background of the spin-flux model is the meron-antimeron pair, for  $3 < U/t < 8$ . At larger  $U/t$ , two charged spin bags become more stable, in the static HF approximation. This is in close analogy to the prediction that the spin bag is energetically more favorable than the static charged domain wall for  $U/t > 6.5$ , in the HFA of the 1D Hubbard model.<sup>3</sup> However, in the 1D case the charged domain wall is considerably more mobile than the charged spin bag, gaining a kinetic energy on the order of  $t$  as opposed to  $t^2/U$  energy gained by the spin bag. As a result, when this kinetic energy of deconfinement is taken into account within the CI method, the charged domain wall is found to be the relevant charged excitation for all values of  $U/t$ . A similar picture emerges in the 2D case, because the meron vortices are much more mobile than the spin bags.

For the 2D system, we have shown that the charged spin bag has a behavior very similar to that of the 1D charged spin bag. The analog of the 1D charged bosonic domain wall is the 2D charged bosonic meron vortex. We now consider the properties of the doubly charged meron-antimeron pair. All the numerical results quoted in the rest of this section refer to a meron-antimeron pair on a  $10 \times 10$  lattice, in the spin-flux model with  $U/t=5$ .

As already discussed, the meron-antimeron pair is not rotationally invariant. We can find the rotational kinetic energy saved by the pair as it rotates about its center of mass. In the present case, only four configurations need to be included, corresponding to the four possible self-consistent arrangements of the meron and antimeron about their fixed center of mass (see Fig. 9). A simple rotation by  $\pi/2$  of the one-particle orbitals  $\phi_p(i, \sigma)$  about the center of mass is not, however, sufficient to generate the rotated configurations. First of all, the  $\pi/2$  rotation also changes the spin-flux parametrization. If the spin flux of the initial configuration is  $T^{12} = -1$  and  $T^{23} = T^{34} = T^{41} = 1$ , a  $\pi/2$  rotation leads to a state corresponding to the rotated configuration  $T^{12} = 1, T^{23}$

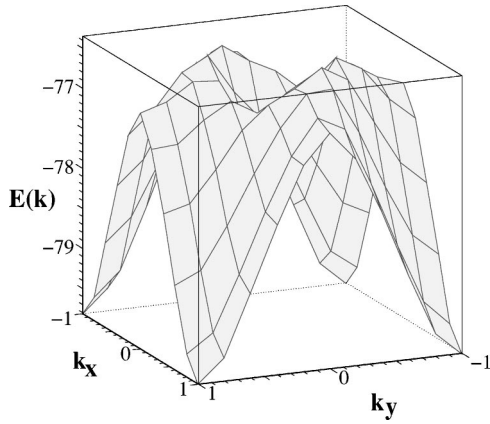


FIG. 10. Total energy  $E(\vec{k})$  (in units of  $t$ ) vs  $\vec{k}$  of the lattice with a (unrotated) meron-antimeron pair as a function of the total momentum  $\vec{k}$  of the pair. The momentum units are  $\pi/a$ . The HF energy of the static meron-antimeron pair is  $-78.52t$ . Quantum hopping lowers the overall energy of the pair by  $1.29t$ . Since the meron-antimeron configuration is not rotationally invariant, the dispersion relation is also not invariant to  $\pi/2$  rotations.

$= -1$ , and  $T^{34} = T^{41} = 1$ . Thus, following the  $\pi/2$  rotation, a unitary transformation must be performed in order to restore the initial spin-flux parametrization. For the case cited above, this simply implies the change in the one-particle orbitals  $\phi_p(i_x, i_y, \sigma) \rightarrow -\phi_p(i_x, i_y, \sigma)$  for all sites  $(i_x, i_y)$  which are a type '2' site of the unit cell, in other words sites with even  $i_x$  and odd  $i_y$  (also see Fig. 1). The second observation is that the rotation by  $\pi/2$  also changes (flips) all the spins of the AFM background surrounding the pair. Thus an extra  $\pi$  rotation about an axis perpendicular to the lattice plane is necessary to restore the alignment of the AFM background. Following these transformations it is straightforward to generate the Slater determinants  $|\Psi_2\rangle, |\Psi_3\rangle$  and  $|\Psi_4\rangle$  corresponding to the meron-antimeron pairs rotated by  $\pi/2, \pi$ , and  $3\pi/2$  from the initial self-consistent HF meron-antimeron pair described by  $|\Psi_1\rangle$ . The CI method can be used to find the rotational energy saved by superposing these rotated meron-antimeron configurations. The lowest CI energy found is  $0.46t$  below the energy of the static pair, and corresponds to  $d$ -wave symmetry. By this we mean that the coefficients  $\alpha_i$ , multiplying the four rotated states in the CI wave function  $|\Psi\rangle = \sum_{i=1}^4 \alpha_i |\Psi_i\rangle$ , satisfy the condition  $\alpha_1 = -\alpha_2 = \alpha_3 = -\alpha_4$ .

Translation of a pair over the whole lattice can also be investigated. Since the pair does not carry any spin, all possible translations must be included (there is no restriction to the same magnetic sublattice configurations). This leads to a total of  $N^2$  possible configurations for an  $N \times N$  lattice. Again, when various configurations are generated from the initial self-consistent HF meron-antimeron state  $|\Psi_1\rangle$ , care must be taken to preserve the same spin-flux parametrization and the same AFM background orientation. This can be achieved by performing transformations similar to the ones described above. As a result of performing the CI method on the set of translated states, we find the dispersion relation of the (unrotated) meron-antimeron pair. This is shown in Fig. 10. In this plot we show the total energy of the lattice with the moving meron-antimeron pair, as a function of the total momentum of the pair. Quantum hopping of the meron-

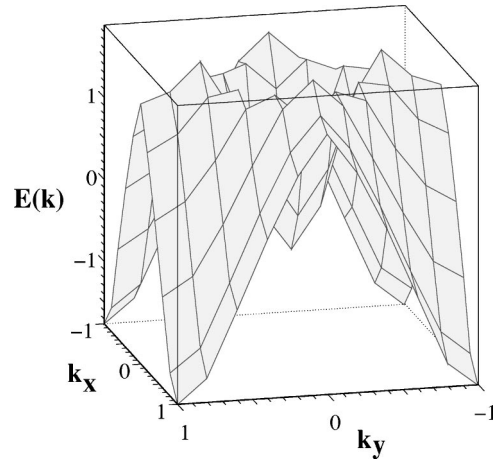


FIG. 11. The lowest-energy dispersion band  $E_{pair}(\vec{k})$  (in units of  $t$ ) as a function of the total momentum  $\vec{k}$  of the meron-antimeron pair. The momentum units are  $\pi/a$ . For convenience, the reference energy is taken to be the static HF energy of the self-consistent meron-antimeron pair. Quantum hopping and rotation lowers the overall energy of the pair by  $1.75t$ . The rotational symmetry of the dispersion relation is restored (compared to Fig. 10).

antimeron pair lowers its total energy by an extra  $1.29t$ . Two other interesting features are observed in Fig. 10. The first one is that the dispersion relation of this rigidly polarized pair is not invariant to rotations by  $\pi/2$ , as expected. More important is that the minima of the dispersion relation occur at the  $(\pi, \pi)$  points. Since the momentum of the pair is twice the momentum of either the meron or the antimeron, this is consistent with the fact that, in their lowest-energy state, both the meron and antimeron have momenta of  $(\pi/2, \pi/2)$  in the spin-flux model. The doubling of the size of the Brillouin zone is also a direct consequence of this doubling of the total momentum (for comparison with undoped dispersion relation, see Fig. 2).

However, to obtain the true energy of the charged pair, we must mix all  $4N^2$  rotated and translated meron-antimeron configurations. All have the same static HF energy and are equally important in the CI method. Let  $|\Psi_0(0,0)\rangle$  denote the initial self-consistent static Hartree-Fock meron-antimeron configuration, and  $|\Psi_\theta(n,m)\rangle$  denote the configuration obtained through translation by  $n$  sites in the  $x$  direction and  $m$  sites in the  $y$  direction, as well as a rotation by an angle of  $\theta(\pi/2)$  of the pair about its center of mass. Here  $0 \leq \theta \leq 3$  and  $0 \leq n \leq N-1, 0 \leq m \leq N-1$  (cyclic boundary conditions are imposed). The CI wave functions are then given by

$$|\Psi_{\vec{k}}\rangle = \sum_{(n,m)} e^{i(k_x n + k_y m)a} \left( \sum_{\theta=0}^3 \alpha_\theta |\Psi_\theta(n,m)\rangle \right). \quad (21)$$

The dispersion relation

$$E_{pair}(\vec{k}) = \frac{\langle \Psi_{\vec{k}} | \mathcal{H} | \Psi_{\vec{k}} \rangle}{\langle \Psi_{\vec{k}} | \Psi_{\vec{k}} \rangle} - E_{pair}^{HF},$$

obtained from this complete set, is shown in Fig. 11. The reference point is the HF energy of the self-consistent meron-antimeron pair  $E_{pair}^{HF} = -78.52t$ . Thus we see that the

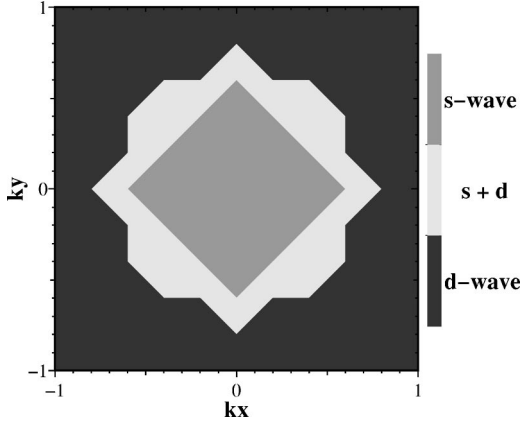


FIG. 12. The rotational symmetry of the meron-antimeron wave function as a function of the total momentum carried by the pair (measured in units of  $\pi/a$ ). The outside region [containing the absolute minima points  $(\pi, \pi)$ ] has *d*-wave symmetry ( $J=2$ ), while the core region about the  $(0,0)$  point has an *s*-wave symmetry ( $J=0$ ). The intermediary area is a mix of  $(s+d)$ -wave symmetry.

total kinetic energy saved by the freely moving and rotating meron-antimeron pair is  $1.75t$ , when the total momentum of the pair is  $(\pi, \pi)$ . This energy equals the sum  $0.46t + 1.29t$  of rotational and translational kinetic energies found before (the number of significant figures indicates the estimated accuracy of the computational method). The rotational invariance of the dispersion band is also restored. Besides the absolute minima about the  $(\pi, \pi)$  points, there is a more shallow minimum region about the  $(0,0)$  point.

The rotational symmetry of the meron-antimeron pair wave function, defined by the coefficients  $(\alpha_\theta)$ , is a function of the total momentum carried by the pair, as shown in Fig. 12. The absolute minima points  $(\pi, \pi)$  and the area around them correspond to pairs with *d*-wave symmetry. By this, we mean that the coefficients  $\alpha_\theta$  have the form

$$\alpha_\theta = \exp\left(iJ\theta\frac{\pi}{2}\right)\alpha_0, \quad (22)$$

with  $J=2$ , i.e.,  $\alpha_0 = -\alpha_1 = \alpha_2 = -\alpha_3$ . The core area, about the local minimum  $(0,0)$  point, corresponds to *s*-wave symmetry. In this region the coefficients  $(\alpha_\theta)$  again satisfy Eq. (22), but for  $J=0$ , i.e.,  $\alpha_0 = \alpha_1 = \alpha_2 = \alpha_3$ . The intermediary area appears to be a mixture of different  $J$  values. A simple decomposition of the form of Eq. (22) is no longer possible. Instead, a sum of such terms corresponding to different  $J$  values is required. Since we only have rotations by  $\pi/2$ , a unique identification of the composite symmetry is not possible. Moreover, the energy of the states in this intermediary area is at the top of the dispersion band. In order to find the correct CI states for energies well above the static HF value (i.e., larger than zero, in this case) we must add to the CI set the first set of excited HF states. For a meron-antimeron pair, excitation of an electron from the valence band onto the empty localized levels inside the Mott-Hubbard gap costs about  $1.5t$  of energy, for  $U/t=5$ , so such states should contribute significantly in the CI states with positive energies and modify their dispersion and symmetry (for this reason, we do not show the upper three high-energy bands in Fig. 11). Consequently, both the energy and symmetry of the

states in the intermediate area may be modified from the ones shown in Fig. 11. However, the minima at  $(\pi, \pi)$  and  $(0,0)$  are at energies well below zero. Their energies and rotational symmetry are unaffected by additions of higher-energy configurations to the CI set.

The fact that we obtain two distinct minima is not very surprising. As argued above, we expect that individual merons and antimerons are created with momenta of  $(\pm\pi/2, \pm\pi/2)$ . As a result, two different couplings are possible. A  $(\pi/2, \pi/2)$  meron can pair with a  $(\pi/2, \pi/2)$  antimeron, creating a pair of total momentum  $(\pi, \pi)$ . This is the most stable coupling, leading to the lowest possible energy of  $-1.75t$  below the static HF energy. This pair has *d*-wave symmetry. The second possible coupling is between a  $(\pi/2, \pi/2)$  meron and a  $(-\pi/2, -\pi/2)$  antimeron. This pair has a total momentum of  $(0,0)$ , and *s*-wave symmetry. However, this coupling is less strong. For the  $U/t=5$  case considered, the energy of the *s*-wave  $(0,0)$  pair is  $1.28t$  above the energy of the *d*-wave  $(\pi, \pi)$  pair. The existence of both *d*- and *s*-wave pairings, and the dominance of the *d*-wave pairing, have been established experimentally for the high- $T_c$  cuprates.<sup>21</sup> We are not aware of any other microscopic theory that predicts the two types of pairing to appear in different regions of the Brillouin zone.

The total kinetic energy saved by the meron-antimeron pair through quantum hopping and rotation is of order  $t$ , as expected, since the pair is not restricted to one magnetic sublattice, and tunneling is not required for motion. Consequently, we expect that the energy saved by the meron-antimeron pair for larger values of  $U/t$  is comparably large. On the other hand, the energy saved by the spin bag through tunneling motion scales like  $t^2/U$ . In fact, we argued that a spin bag may dissociate into a singly charged vortex-antivortex pair in order to enhance its mobility. However, even if dissociation does not occur, the kinetic energy saved by a pair of spin bags is significantly smaller than the kinetic energy saved by the meron-antimeron pair. This shows that for  $U/t=5$  the meron-antimeron pair is even more favorable energetically than the HFA predicts, and suggests that the  $U/t$  range where meron-antimeron pair formation occurs may extend well beyond the  $U/t=8$  limit found within the HFA.<sup>9</sup> In the 1D case, the range of stability of the charged domain wall versus the charged spin bag is extended (from the HF prediction of  $U/t=6.5$ ) to all  $U/t$  ranges.<sup>3</sup> A numerical analysis is needed to determine if the limit is extended to infinity in the 2D case as well.

## V. SUMMARY AND CONCLUSIONS

The configuration-interaction approximation incorporates crucial quantum translational and rotational motion of the charge carriers, which are absent in the static Hartree-Fock approximation. Given the accuracy of the CI method in recapturing certain features of the exact Bethe ansatz solution of the 1D Hubbard model,<sup>3</sup> we believe that the CI method is likewise a very powerful tool for describing effects beyond mean-field theory in two dimensions. For 2D systems, numerical calculations are much more time consuming. However, our small sample of results is quite suggestive of a simple physical picture. In direct analogy with the 1D re-

sults, we find that the bosonic charged meron vortices are much more mobile than the fermionic charged spin bags. The extra kinetic energy gained by the meron vortices very likely extends their region of stability beyond the  $U/t=8$  limit suggested in the HFA.<sup>9</sup> There are also strong indications that a charged spin bag is unstable to decay into a singly charged bound vortex-antivortex pair. This appears to be a 2D precursor to the spin-charge separation in the 1D case. Nucleation of such pairs of vortices with doping is expected to further influence the magnetic behavior of the cuprates. The bound state and the unbound continuum states of the singly charged meron-antimeron pair may account for the anomalous “quasiparticle” spectral widths observed on angle-resolved photoemission experiments.

The symmetry of the meron-antimeron pairs emerges very clearly from the CI treatment. We find two regions of stability of the meron-antimeron pair. Pairs with a total momentum of  $(\pi, \pi)$  have  $d$ -wave symmetry, and are the most stable. Pairs with a total momentum  $(0,0)$  have  $s$ -wave symmetry and have a smaller gap. Thus we find that different pairing appears in different regions of the Brillouin zone. These results appear to have a direct bearing on numerous experiments, which show a mixture of a strong  $d$ -wave component and a smaller  $s$ -wave component in the superconducting state of the cuprates.<sup>21</sup>

Many other features of our model are in agreement with experimentally observed properties of the cuprate superconductors. Nucleation of magnetic vortices with doping explains a variety of magnetic properties, starting with complete destruction of the long-range AFM order for very low doping concentration. As we can see from Fig. 5(a), a tightly bound meron-antimeron pairs disturbs the long-range AFM ordering of most of the spins on the  $10 \times 10$  lattice. For very low dopings, these pairs are far from each other, and there are many spins on the plane whose orientations are not affected by any pair. Thus most of the spins maintain long-range AFM order. However, as the doping increases to about 5% (which is roughly equivalent to having two meron-antimeron pairs on the  $10 \times 10$  lattice) the areas occupied by each meron-antimeron pairs start to overlap with those occupied by the neighboring pairs. At this doping the orientation of all the spins on the  $\text{CuO}_2$  planes is affected by at least one pair of vortices, and therefore the long-range order (LRO) is severely disrupted. The local ordering, however, is still AFM. This picture explains the extremely low doping necessary for the disappearance of LR AFM order, as well as the fact that the spin correlation length is basically equal to the average distance between holes (vortices) and does not depend strongly on the temperature.<sup>22</sup> Each hole carries its vortex with it, and the spins in each vortex are correlated with each other. The correlation length is thus roughly equal to the average size of the vortex which is defined by the average intervortex (interhole) distance. The nucleation of magnetic vortices also explains the split of the  $(\pi, \pi)$  AFM Bragg peak into the four incommensurate peaks whose positions shift with doping,<sup>23</sup> as observed in LaCuO and, more recently, in YBaCuO.<sup>24</sup> The form factor of any given vortex already gives rise to an apparent splitting of the neutron scattering peak. As demonstrated in Ref. 9, even at the mean-field level we recapture the neutron scattering data using a random distribution of meron vortices.

The optical behavior of the cuprates is also explained naturally using our model. Two features develop in the optical-absorption spectra with doping: a broad midinfrared temperature-independent absorption band, and a strongly temperature-dependent low-frequency Drude tail.<sup>25</sup> In our model the broad midinfrared band is related to the excitation of electrons from the valence band onto the empty levels bound in the vortex cores,<sup>9</sup> which are localized deep inside the Mott-Hubbard gap [see Fig. 4(b)]. The number of localized levels scales with the number of vortices, and intervortex interactions lead to their splitting into a broad band. As such, this mechanism is similar to the one leading to a broad midinfrared absorption band in polyacetylene with doping.<sup>26</sup> The polyacetylene band is due to electronic excitations inside the cores of the polyacetylene domain-wall solitons,<sup>19</sup> which are the topological analogues of meron vortices.<sup>12,13</sup> Another strong argument in favor of this interpretation is provided by photoinduced absorption experiments.<sup>27</sup> If the undoped parent compounds are illuminated with intense visible light, they develop absorption bands that resemble the midinfrared bands of the doped compounds. A similar behavior is observed in polyacetylene, and is attributed to the nucleation of solitons by photoexcited electron-hole pairs.<sup>28</sup> The second component of the optical spectrum is the Drude tail. It results from the response of the freely moving charged vortices to the external electric field. The strong temperature dependence of this tail is determined by the scattering mechanism for merons (presumably due to interactions with other merons and spin waves). This interpretation is also supported by the fact that the superconducting transition leaves the midinfrared absorption band unchanged. Merons with internal electronic structure are still present on the planes, but pair condensation leads to a collapse of the Drude tail into a  $\delta(\omega)$  response.

As already discussed, nucleation of charged meron vortices with doping provides a microscopic basis for non-Fermi-liquid behavior, due to the bosonic nature of the mobile charged excitations. The model also predicts the existence of preformed pairs with  $d$ -wave symmetry, which are thought to be responsible for the pseudogap effects.<sup>29</sup> As the number of pairs of charged bosons increases with doping and the temperature is lowered, the meron-antimeron pairs Bose condense and become coherent, leading to superconductivity. This mechanism naturally explains the puzzling scaling of the superfluid density with doping  $\rho_s \sim \delta$ , in other words with the number of holes, not of electrons. In our model, it is the doping-induced positively charged meron vortices that are the mobile charge carriers. As a result, the density of preformed meron-antimeron Cooper pairs is obviously proportional to doping. Finally, for large dopings ( $\delta > 0.30-0.40$ ) the average vortex size become extremely small, and the very cores of the merons start to overlap. In this limit the Mott-Hubbard gap is completely filled in by the discrete levels, and the spin-flux state becomes energetically unstable relative to a normal Fermi liquid.<sup>9</sup>

It is noteworthy that all of the independent features described above are in qualitative agreement with our model, which has essentially no free or adjustable parameters. The choice of  $U/t$  is fixed by the experimentally measured size of the Mott-Hubbard charge-transfer gap at zero doping. More detailed comparisons with specific experiments may require

the incorporation of specific (smaller energy scale) interactions which are not included in this simplest version of the spin-flux Hamiltonian. A derivation of the explicit consequences of this picture appears to be worthy. A more comprehensive and quantitative comparison with the experiments may prove quite fruitful.

## ACKNOWLEDGMENTS

M.B. acknowledges support from the Ontario Graduate Scholarship Program, and a fellowship from William F. McLean. This work was supported in part by the Natural Sciences and Engineering Research Council of Canada.

- 
- <sup>1</sup>P.W. Anderson, *Science* **235**, 1196 (1987).
- <sup>2</sup>See, for instance, D.M. Ginsberg, *Physical Properties of High Temperature Superconductors* (World Scientific, Singapore, 1992), Vols. I–V.
- <sup>3</sup>M. Berciu and S. John, *Phys. Rev. B* **61**, 10 015 (2000); [cond-mat/9912460 (unpublished)].
- <sup>4</sup>D. Poilblanc and T.M. Rice, *Phys. Rev. B* **39**, 9749 (1989); H.J. Schultz, *J. Phys. (Paris)* **50**, 2833 (1989).
- <sup>5</sup>M. Kato, K. Machida, H. Nakanishi, and M. Fujita, *J. Phys. Soc. Jpn.* **59**, 1047 (1990); K. Machida, *Physica C* **158**, 192 (1989).
- <sup>6</sup>J. Zaanen and O. Gunnarson, *Phys. Rev. B* **40**, 7391 (1989); J. Zaanen, M.L. Horbach, and W. van Saarloos, *ibid.* **53**, 8671 (1996).
- <sup>7</sup>V.J. Emery and S.A. Kivelson, *Nature (London)* **374**, 4347 (1995); V.J. Emery, S.A. Kivelson, and O. Zachar, *Phys. Rev. B* **56**, 6120 (1997).
- <sup>8</sup>S. John and A. Golubentsev, *Phys. Rev. Lett.* **71**, 3343 (1993); *Phys. Rev. B* **51**, 381 (1995).
- <sup>9</sup>Mona Berciu and Sajeev John, *Phys. Rev. B* **59**, 15 143 (1999).
- <sup>10</sup>E. Louis, F. Guinea, M.P. Lopez Sancho, and J.A. Verges, *Phys. Rev. B* **59**, 14 005 (1999).
- <sup>11</sup>E.H. Lieb and F.Y. Wu, *Phys. Rev. Lett.* **20**, 1445 (1968).
- <sup>12</sup>S. John, M. Berciu, and A. Golubentsev, *Europhys. Lett.* **41**, 31 (1998).
- <sup>13</sup>M. Berciu and S. John, *Phys. Rev. B* **57**, 9521 (1998).
- <sup>14</sup>S. John and A. Müller-Groeling, *Phys. Rev. B* **51**, 12 989 (1995).
- <sup>15</sup>N.E. Bonesteel, T.M. Rice, and F.C. Zhang, *Phys. Rev. Lett.* **68**, 2684 (1992).
- <sup>16</sup>P. Fulde, *Electron Correlations in Molecules and Solids*, (Springer, 1995).
- <sup>17</sup>B.O. Wells, Z.-X. Shen, A. Matsuura, D.M. King, M.A. Kastner, M. Greven, and R.J. Birgeneau, *Phys. Rev. Lett.* **74**, 964 (1995).
- <sup>18</sup>S. LaRosa, I. Vobornik, F. Zwick, H. Berger, M. Grioni, G. Margaritondo, R.J. Kelley, M. Onellion, and A. Chubukov, *Phys. Rev. B* **56**, R525 (1997); C. Kim, P.J. White, Z.-X. Shen, T. Tohyama, Y. Shibata, S. Maekawa, B.O. Wells, Y.J. Kim, R.J. Birgeneau, and M.A. Kastner, *Phys. Rev. Lett.* **80**, 4245 (1998).
- <sup>19</sup>A.J. Heeger, S. Kivelson, J.R. Schrieffer, and W.-P. Su, *Rev. Mod. Phys.* **60**, 781 (1988).
- <sup>20</sup>W.-P. Su, J.R. Schrieffer, and A.J. Heeger, *Phys. Rev. B* **22**, 2099 (1980).
- <sup>21</sup>D.J. Van Harlingen, *Rev. Mod. Phys.* **67**, 515 (1995).
- <sup>22</sup>R.J. Birgeneau and G. Shirane, in *Physical Properties of High Temperature Superconductors I*, edited by Donald M. Ginsberg, (World Scientific, Singapore, 1989).
- <sup>23</sup>K. Yamada, C.H. Lee, K. Kurahashi, J. Wada, S. Wakimoto, S. Ueki, H. Kimura, Y. Endoh, S. Hosoya, G. Shirane, R.J. Birgeneau, M. Greven, M.A. Kastner, and Y.J. Kim, *Phys. Rev. B* **60**, 6165 (1998); D. Vaknin, S. K. Sinha, D. E. Moncton, D. C. Johnston, J. M. New, C. R. Safinya, and H. E. King, Jr., *Phys. Rev. Lett.* **58**, 2802 (1987).
- <sup>24</sup>M. Arai, T. Nishijima, Y. Endoh, T. Egami, S. Tajima, K. Tomimoto, Y. Shiohara, M. Takahashi, A. Garrett, and S.M. Bennington, *Phys. Rev. Lett.* **83**, 608 (1999).
- <sup>25</sup>For a review of optical properties, see D.B. Tanner and T. Timusk, in *Physical Properties of High Temperature Superconductors III*, edited by Donald M. Ginsberg (World Scientific, Singapore, 1992); G.A. Thomas, in *High Temperature Superconductivity*, edited by D.P. Tunstall and W. Barford, Proceedings of the 39th Scottish Universities Summer School in Physics, St. Andrews (Hilger, New York, 1991).
- <sup>26</sup>J. Tanaka and M. Tanaka, *Optical Spectra of Conducting Polymers in Handbook of Conducting Polymers II*, edited by T.A. Skotheim (Dekker, New York, 1986).
- <sup>27</sup>C.M. Foster, A.J. Heeger, G. Stuckey, and N. Heron, *Solid State Commun.* **71**, 945 (1989).
- <sup>28</sup>J. Orenstein, *Photoexcitation of Conjugated Polymers in Handbook of Conducting Polymers II* (Ref. 26).
- <sup>29</sup>See, for instance, T. Timusk and B. Statt, *Rep. Prog. Phys.* **62**, 61 (1999).